Modification of electronic and thermoelectric properties of InSe/GaSe superlattices by strain engineering

Wilfredo Ibarra-Hernández [1,*], A. C. Garcia-Castro [2], Alejandro Bautista-Hernández [1], Martin Salazar-Villanueva [1], Andrés Cantarero [3] and Aldo H. Romero [4,1,5]

[1]*Facultad de Ingeniería, Benemérita Universidad Autónoma de Puebla, Apdo. Postal J-39, Puebla, Pue. 72570, Mexico*
[2]*School of Physics, Universidad Industrial de Santander, Carrera 27 Calle 9, 680002 Bucaramanga, Colombia*
[3]*Institut de Ciència Molecular, Universitat de València, P.O. Box 22085, 46071 Valencia, Spain*
[4]*Department of Physics and Astronomy, West Virginia University, Morgantown, West Virginia 26506-6315, USA*
[5]*Department of Physics and Materials Science, University of Luxembourg, 1511 Luxembourg, Luxembourg*

In recent years, superlattices and layered materials have been highlighted as potential candidates for thermoelectric applications, this thanks to their low thermal conductivity. Moreover, external applied pressure and biaxial strain can be used to enhance their properties by achieving a band engineering and electronic tuning. With this in mind, we performed an *ab initio* based study on InSe/GaSe superlattices under biaxial strain along the layer planes. Layers of InSe and GaSe with D_{3h} symmetry were stacked along the c axis to create the superlattice. The atomic stacking along the c axis is Se-Ga-Ga-Se-Se-In-In-Se, which corresponds to the space group #187. Our *ab initio* calculations predict the superlattice to be a semiconductor with an electronic band gap of $E_g = 0.54$ eV. With the aim to increase thermoelectric performance, we apply positive and negative biaxial strain on the *ab* plane. Under compressive strain, the electronic structure evolves to an insulating behavior by increasing the band gap. When tensile strain is applied, we observe a transition towards a metallic character with a systematic reduction of the band gap. Interestingly, the semiconductor-metal transition only occurs when spin-orbit coupling (SOC) is switched off. With the inclusion of SOC, the system experiences an electronic topological transition around 3% tensile strain, with a double band gap along the K-Γ-M high-symmetry paths. We have found that for both, *n*-type and *p*-type doping, compressive strain improves the electronic figure of merit (ZT_e under constant relaxation time approximation). Not only the electronic part increases thermoelectric performance, but also the lattice contribution to the thermal conductivity decreases with compressive strain.

I. INTRODUCTION

In our quest for new, renewable, and clean energy sources, thermoelectricity stands as an excellent candidate thanks to the numerous sources of wasted heat in devices, the lack of moving parts that minimize maintenance and the existence of materials that potentially can use that energy [1–3]. Even though the first report on the use of thermoelectricity has been known for over 60 years [3], the low efficiency of thermoelectric materials has limited its usage to concrete applications, especially in those where cost is not an issue [4,5]. The other drawback of thermoelectricity is the high cost of the materials that exhibit the best thermoelectric performance. For example, despite bismuth telluride, Bi_2Te_3, remains as one of the best bulk thermoelectric materials at low temperatures (around 320 K) [6], tellurium is a scarce element, and its inclusion increases the cost of thermoelectric devices [7]. Therefore, the investigation and development of novel materials at affordable cost and enhanced thermoelectric performance is of crucial importance [8,9]. Under these considerations, SnSe was discovered and highlighted as the new state-of-the-art bulk thermoelectric material ($ZT \approx 2.6$ at 923 K) [10–12]. *Ab initio* calculations suggest that the high thermoelectric efficiency of SnSe is mainly due to a one order increase in the carrier concentrations due to Sn vacancies [13] while the ultralow thermal conductivity is a consequence of nonperturbative anharmonicity in the second-order transition from *Cmcm* to the *Pnma* phase [14]. Moreover, tin and selenium are cheap elements, and the thermoelectric performance is high.

In terms of the physical phenomenon involved, the thermoelectric efficiency is characterized by the so-called thermoelectric figure of merit, which is a dimensionless quantity that helps us to measure thermoelectric efficiency. The figure of merit (ZT) considers the material's intrinsic transport properties to quantify the efficiency. The equation is $ZT = T S^2 \sigma / \kappa_t$, where S is the Seebeck coefficient, σ is the electrical conductivity, and κ_t is the total thermal conductivity of the material. κ_t is the sum of the thermal conductivity due to electrons (κ_e) and phonons (κ_p), while T is the absolute temperature. From the previous equation, it is easy to see that the problem in thermoelectricity boils down to maximizing efficiency. Therefore, the thermoelectric performance comes from the properties involved in the figure of merit. All the properties are related to each other, and the increase in one of them usually decreases the other. The Seebeck coefficient, for

*wilfredo.ibarra@correo.buap.mx

example, reaches its maximum value in the middle of the band gap, but at this point, the electrical conductivity is zero. On the other hand, an increase in the electrical conductivity will increase the electronic contribution to the thermal conductivity. As such, the difficulty of increasing ZT lies in the problem of keeping a low thermal conductivity while increasing S (or σ) [15].

As a path to engineering an enhanced thermoelectric response, the growth of superlattices has been suggested. Such superlattices could reduce phonon mean free path and therefore decrease the lattice thermal conductivity [16]. Through the periodic stacking of Bi_2Te_3 and Sb_2Te_3, the thermal conductivity was reduced to 0.22 $W\,m^{-1}K^{-1}$ in the stacking direction [17]. In our previous work, the semiconductor nature of the InSe/GaSe superlattice was confirmed by *ab initio* calculation [18]. InSe/GaSe heterostructures were experimentally grown via mechanical exfoliation, and stacking of the two-dimensional (2D) monochalcogenides InSe and GaSe was demonstrated [19]. However, several new experimental techniques could potentially be suitable to grow InSe/GaSe superlattices [20–22]. With regard to the induction of biaxial strain, the stacking of InSe layers on top of GaSe exhibit a hexagonal structure, which makes it easier to find a substrate that can induce the required strain to tune specific properties of the superlattice. The system could be grown on top of a cubic substrate oriented in the (111) plane. For example, GaSe (monolayer used in our theoretical heterostructure) has been grown on top of Si(111) [23–25], as well as on top of GaAs(111) [26,27]. If InSe/GaSe heterostructure can grow on top of either of these two substrates, there will be a strain of approximately $\pm 2\%$ (+ for tensile on GaAs and − for compressive on Si). It has been reported that electronic and thermoelectric properties (such as Seebeck coefficient) can be tuned through biaxial mechanical strain [28,29]. Not only the electronic-related properties can be modified via strain, but it was also theoretically predicted that the thermal conductivity of monolayers of InSe could be drastically reduced via biaxial strain [30].

This work presents our results on the *ab initio* calculations for thermoelectric and electronic properties of the InSe/GaSe superlattices under the effects of biaxial strain. Aside from the thermoelectric properties, we have found that under the effect of positive biaxial strain (tensile strain), the superlattice exhibits a band crossing. Interestingly, the band crossing disappears, and a gap opens at the band crossing when spin-orbit coupling (SOC) is considered. We follow the changes in the thermoelectric properties through these changes in the electronic topology. We observed that with tensile strain, the increase in σ is not enough to overcome the decrease in S and there is a constant reduction on the electronic figure of merit (ZT_e) with strain.

II. COMPUTATIONAL DETAILS

We performed *ab initio* calculations for InSe/GaSe superlattices. The stacking sequence along the c axis is Se-Ga-Ga-Se-Se-In-In-Se, while the resulting symmetry is that corresponding to the space group #187. The compressive (tensile) biaxial strain was induced by a reduction (increment) of the a and b parameters while the c parameter was allowed

to relax fully. The calculations were performed from the fully relaxed structure (0% strain) up to +5% (tensile strain) and −5% (compressive strain) in 1% steps. We have used the Vienna *ab initio* simulation package (VASP version 5.4.4) [31] which works in the framework of density functional theory (DFT) [32,33] and the projected augmented-wave method [34]. The exchange-correlation functional used corresponds to the general gradient approximation (GGA) to the exchange-correlation energy and the Perdew-Burke-Ernzerhof corrected for solids (PBEsol) functional [35]. The chosen pseudopotentials consider 3 ($5s^25p^1$, version 08Apr2002), 13 ($3d^{10}4s^24p^1$, version 06Jul2010), and 6 ($4s^24p^4$, version 06Sep2000) valence electrons for In, Ga, and Se atoms, respectively. The plane-wave energy cutoff was set to 550 eV to ensure that the forces between atoms were not higher than 10^{-5} eV/Å. The maximum remanent strain allowed during relaxation was set to 5×10^{-4} kbar in all directions for the fully relaxed system. The reciprocal space was integrated with a Monkhorst-Pack [36] grid of $8 \times 8 \times 4$ centered at the Γ point. This grid was used in stress and atomic forces relaxation.

For non-self-consistent calculations, the density of the K-mesh grid was increased up to $16 \times 16 \times 8$. To corroborate values of the electronic band gap, we have used the newly implemented capabilities in the VASP code that allow us to perform metaGGA calculations [more explicitly the "strongly constrained and appropriately normed" (SCAN)] [37]. We perform relaxation of the cell and electronic band structure calculations with SCAN only for specific values of strain and for the fully relaxed structure. We have also calculated the electronic band gap for the fully relaxed system using the modified Becke-Johnson exchange potential [38,39]. The use of this last functional is to obtain a better estimation of the electronic band gap.

For the calculation of thermoelectric properties, we have used the second version of the BOLTZTRAP code (BTP2) [40]. This software solves the Boltzmann transport equations for electrons to obtain the Seebeck coefficient explicitly. It is also possible to calculate the electrical conductivity under the constant relaxation time approximation (σ/τ). To simulate different doping levels, the code uses the rigid band approximation, which assumes that under small doping values, the shape of the band will remain unchanged, and the chemical potential will be shifted to either inside the valence (p-type doping) or the conduction (n-type doping) bands. This approximation has proven to be accurate for well-known semiconductors such as Bi_2Te_3 and Sb_2Te_3, among others [41,42].

Phonon dispersions and second-order interatomic force constants (IFCs) were calculated with the PHONOPY package [43] without the inclusion of SOC. The supercell used for phonon band structure and second-order IFCs was $4 \times 4 \times 2$. To obtain the lattice contribution to the thermal conductivity, the SHENGBTE code was used [44,45]. SHENGBTE needs the third-order interatomic force constants to solve the Boltzmann transport equation for phonons. In order to calculate the third-order IFCs, it is necessary to compute the energy in distorted supercells. The thirdorder.py script [46] was used to create the distorted structures. The supercell size was $2 \times 2 \times 2$, and it was imposed that interactions up to the tenth neighbor were considered. It is important to include a large number
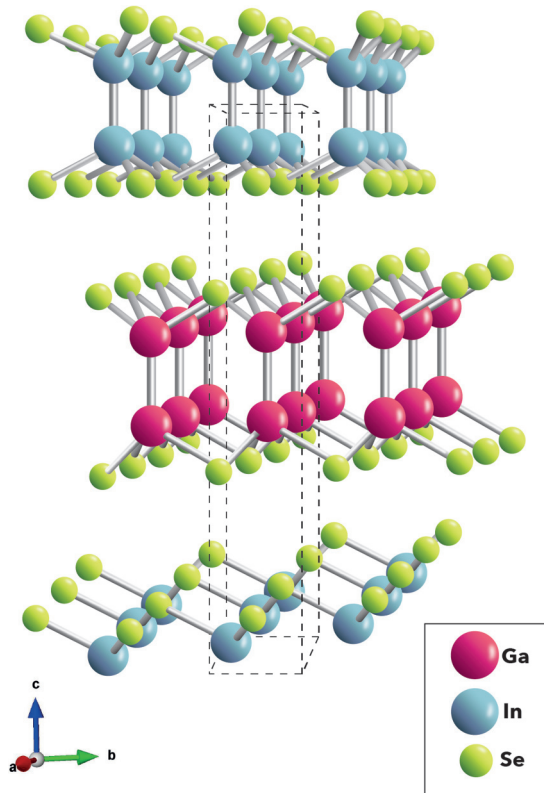
FIG. 1. InSe/GaSe Superlattice. In, Ga, and Se atoms are represented by blue, pink, and green balls, respectively. The primitive cell has been expanded for a better representation of the layered nature of the superlattice.

of neighbors in the calculations since layered systems exhibit strong anharmonicity [47]. The number of individual distorted supercells was up to 768. Thermal conductivity calculations aim to set the overall trend under strain. Therefore, we have only calculated phonons and thermal conductivities for -3%, 0%, and $+3\%$ strain.

III. CRYSTAL STRUCTURE

The obtained superlattice has two formula units per primitive cell with space group #187. Figure 1 depicts a supercell of the structure, expanded along the ab plane for better appreciation. The dashed black line represents the unit cell. The crystal structure was created by stacking the ε polytype of GaSe, but we changed the gallium atom by selenium in one layer. Basically, this structure consists of adjacent layers of Ga-Se and In-Se, as can be seen from Fig. 1. The layers are created so that each In (Ga) atom forms bonds with three Se atoms. Afterward, we have a Ga-Ga (In-In) bond along the stacking axis, and then we have the hexagonal layer of Se atoms. Adjacent layers of Se are weakly bonded, and it is for this reason that the Se-Se distance between layers is more significant than the Se-Se in-plane distance (4.03 Å and 3.97 Å at zero strain, respectively). We choose this configuration since single layers of both compounds have the exact point symmetry (D_{3h}) [48]. However, this similarity between monolayers of GaSe and InSe breaks when the layers form

a bulk system. The GaSe layer stays in the ε polytype while InSe changes to its γ polytype (rhombohedral). The latter is because of the bulklike symmetry of InSe and GaSe that in our proposed superlattice differs from the structure proposed in the work of Gashimzade and Mustafaev [49]. They create a structure where layers of ε-GaSe are stacking on top of layers of γ-InSe.

IV. RESULTS AND DISCUSSION

Before applying the biaxial strain, our calculations should be compared to monolayers of InSe and GaSe. The lattice parameters of the fully relaxed superlattice are $a = b = 3.88$ Å and $c = 16.70$ Å. Concerning the atomic bond lengths, the InSe layer in the InSe/GaSe superlattice has a distance between In-In atoms of 2.76 Å, between In and Se of 2.63 Å, and the monolayer thickness, d, of InSe (i.e., the distance between Se atoms in the In-Se layer) is $d = 5.51$ Å. The atomic distances found in previous works for In-In, In-Se, and Se-Se for the monolayer of InSe are 2.82, 2.69, and 5.39 Å, respectively [50]. For the GaSe layer in the superlattice, the Ga-Ga, Ga-Se, and Se-Se, the distances are 2.44, 2.50, and 4.66 Å, respectively. In the theoretical work of Ma *et al.* [51], the authors report values for the monolayer and bilayer of GaSe. For the monolayer, the authors found that the distances are Ga-Ga = 2.47 Å, Ga-Se = 2.50 Å, and $d = 4.83$ Å. Our results do not differ significantly from those on the monolayers of either Ga-Se or In-Se. However, it is worth mentioning that all our results are reported for the superlattice of InSe/GaSe.

Our calculations show that the InSe/GaSe superlattice is a direct band-gap semiconductor with a higher valence band and a lower conduction band at the Γ point as can be seen in Supplemental Material Fig. S1 [52]. The value of the band gap is 0.544 eV, computed within the used exchange correlation, which is a high value compared to Bi_2Te_3 with a theoretical band gap of around 0.08 eV [42]. This large band gap will have an impact on thermoelectric efficiency. Comparing our results with those in the literature for InSe and GaSe, we have noticed that monolayers of both GaSe and InSe have an indirect band gap. However, in both cases, there are reports of a direct to indirect band-gap transition with exfoliation. Not only that, the transition is accompanied by a significant increase in the band gap [51,53–55]. The theoretical band gap for the superlattice that we have found is smaller than the theoretical band gaps for a monolayer of InSe (1.41 eV) [50] and GaSe (around 2.00 eV) [51,56]. Therefore, InSe/GaSe superlattice behaves as a bulk material since it exhibits a direct band-gap electronic structure at zero pressure. It was expected to be a small band gap compared to the monolayers.

Figure 2 shows the most important changes in the crystal structure with the application of strain. The change in the distance between selenium atoms at adjacent layers (Se-Se) does not change significantly with the contraction of the cell. Under the expansion, the change is around 1.5%, which is not significant. The compressive or tensile strain applied at the ab plane changes the α and β angles (α = Se-In-Se and β = Se-Ga-Se) but have no significant change in the distance between selenium atoms in adjacent layers along the c axis. Therefore, the reduction (increment) of the c parameter is
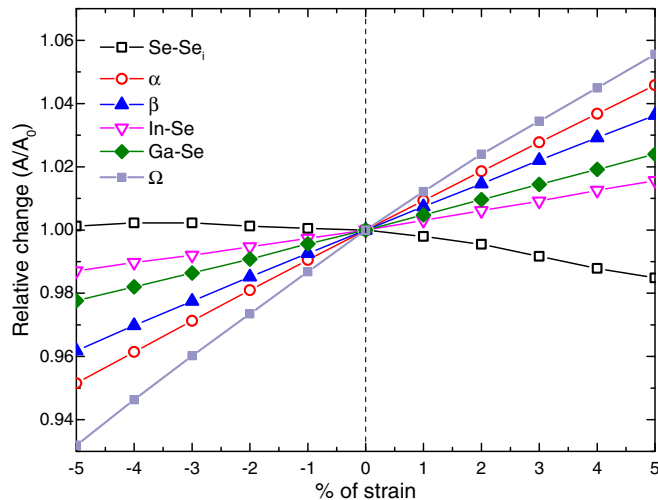
FIG. 2. Relative change of the different distances and angles with respect to those in the fully relaxed structure. We are showing the following: Se-Se interlayer distance, Se-In-Se angle (α), Se-Ga-Se angle (β), In-Se and Ga-Se bond length, as well as the total volume of the cell (Ω).
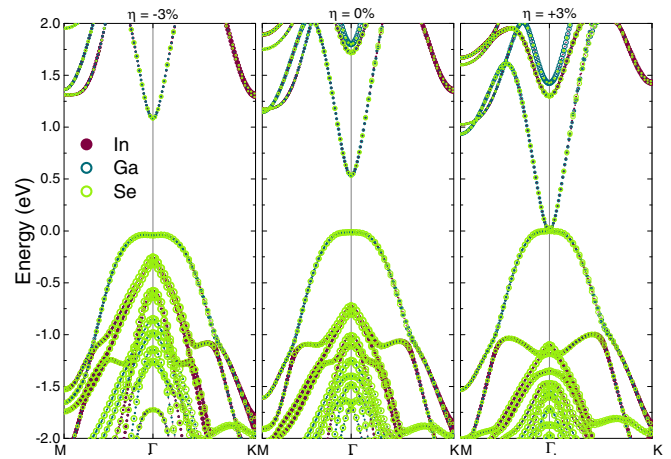

FIG. 3. Projected band structure for InSe/GaSe superlattice with 3% compressive strain (left), fully relaxed (center), and 3% tensile strain (right). The In, Ga, and Se atomic contributions to the band are represented by red, blue, and green circles, respectively.

mainly due to the increase (decrease) of these angles. The Se-Ga-Se (Se-In-Se) angle increases almost 7.4% (9.4%) in the same range from -5% to $+5\%$ strain. The α and β angles are the only ones that change almost the same percentage independently of the applied strain. The atomic distance between subsequent layers of indium is very similar to what has been found in the monolayer of InSe [50]. Our results agree with those reported in the monolayer of InSe, not only in the fully relaxed structure but also under effects of any type of isotropic biaxial strain [50]. Not only the In-In distance remains almost unchanged with the strain but also the Ga-Ga distance. From -5% to $+5\%$, the atomic distance between gallium (indium) atoms in adjacent layers only increases 0.032 Å (0.028 Å), which represents a change of 1.3% (1%) in this range.

With respect to the electronic properties of the InSe/GaSe superlattice under the effects of biaxial strain, the changes are similar to those found in the monolayers of InSe and GaSe. Biaxial compressive strain (negative strain in our calculations) induces an increment in the electronic band gap (see Fig. 3), which is similar to what has been observed in monolayers of InSe. Hu *et al.* [50] report that for InSe, there is a threshold at approximately -4% strain at which the system exhibits an electronic topological transition where the valence band maximum shifts to the Γ point inducing an indirect-direct band-gap transition. TheBInSe/GaSe superlattice is a direct band-gap semiconductor, but when compressive strain is applied, the system shifts its highest valence band along the Γ-K high-symmetry path. On the other hand, under tensile strain, the superlattice remains as a direct band-gap semiconductor up to 3% expansion, as can be observed from Fig. 3.

It has been reported that monolayers of either InSe or GaSe exhibit a reduction of the band gap with increasing strain. Nevertheless, there is a difference between these two systems. *Ab initio* calculations on InSe monolayers show a semiconductor-to-metal transition when the tensile biaxial strain reaches 10% [50]. For GaSe monolayers, this transition

is not theoretically observed at the same 10% of strain [51]. As mentioned, we never observe zero band gap in InSe/GaSe superlattices within the considered strain when SOC is included. Moreover, the electronic band gap increases from 0.017 to 0.051 eV when the strain goes from $+3\%$ to $+5\%$. This behavior is similar to what has been reported for GeTe/Sb$_2$Te$_3$ superlattice under the effect of strain [57]. In their work, Sa *et al.* [57] studied the effect of compressive strain in superlattices of (GeTe)$_2$/Sb$_2$Te$_3$, but the strain was applied to the c axis instead. They reported that under small amounts of compressive strain (2%) along the c axis, the band gap of the superlattice decreases, and at 4%, the gap opens due to SOC effects. The results without SOC show that the system became metallic with a band overlap at Γ, but the inclusion of SOC opens the gap indicating a potential topological insulator behavior for the system under strain. This is very similar to what we have found in InSe/GaSe superlattices. This is not new; it has been reported that for layered bulk GaSe and GaS, the inclusion of strain induces band inversion and when SOC is included the system opens band gaps at the crossing points of the inverted bands [58]. Our work differs from that of Zhu *et al.* [58] since they used experimental values of the cell parameters and the applied strain was induced by variation of the lattice parameter at constant volume; however, their results are very important to understand the effects of strain and SOC on the electronic properties in layered materials.

Figure 4 shows the electronic band structure of the superlattice under the effect of 5% tensile strain with and without the inclusion of SOC. We have included the contribution of the main orbitals to the bands with the aim to identify if the superlattices of InSe/GaSe also have band inversion as a consequence of applied strain. In the left panel of Fig. 4, we observed that applied strain on InSe/GaSe superlattices induces the mentioned band inversion. The inclusion of SOC (right panel) opens the gap at the crossing point of the band inversion, in agreement with the work of Zhu *et al.* for layered GaSe and GaS [58]. Therefore, we never observed the
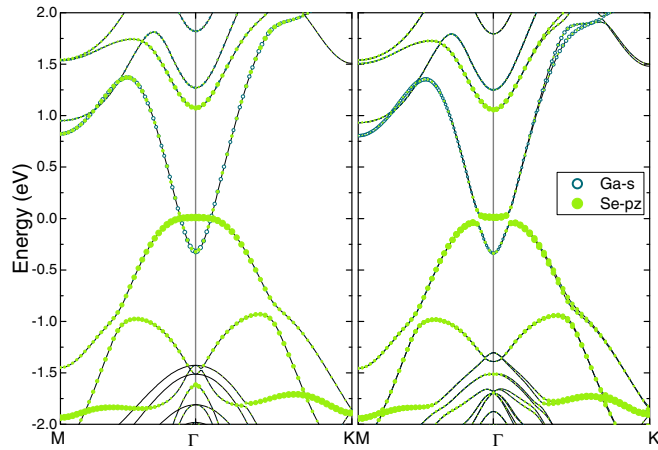
FIG. 4. Projected band structure for InSe/GaSe superlattice under 5% tensile strain without (left) and with (right) SOC. The contribution from s orbitals of Ga atoms and from p_z orbitals from Se atoms are represented by blue open circles and solid green circles, respectively.

FIG. 5. Calculated Seebeck coefficient as a function of the chemical potential for different values of strain at 500 K of temperature.

semiconductor-to-metal transition reported in monolayers of GaSe and InSe [50,51].

Moving forward and analyzing the thermoelectric properties, we notice the metallization of the system will reduce the Seebeck coefficient but, at the same time, will increase the electrical conductivity. Also, the band gap at the crossing points allows more available states around the Fermi level. On the other hand, a larger band gap will increase the Seebeck coefficient, even though the electrical conductivity will decrease. However, before we calculate the thermoelectric properties, it is worth mentioning that DFT systematically underestimates the band gap. Therefore we have used the recently developed SCAN [37] which usually gives a more accurate description of the electronic band-gap energy [59]. The aim of SCAN calculation is none other than to corroborate the results obtained with PBESol with regard to the strain value at which the band crossing without SOC occurs. Therefore, SCAN calculations were only done for specific values of strain (see Fig. S2). The results obtained with SCAN and SOC confirm those obtained with PBESol. The system shows a systematic decrease of the band gap with tensile strain. However, the topological insulator behavior is not present at 5% tensile strain. Therefore, we obtained the SCAN band structure at 6% tensile strain (see Fig. S3). This value of tensile strain was only done to corroborate the topological insulator behavior even with SCAN. Figure S3 compares the 6% SCAN band structure with 5% PBESol where the similarities can be observed.

The calculations of the electronic part of the thermoelectric properties were performed using the BOLTZTRAP2 package [40]. Figure 5 shows the trace of the Seebeck coefficient as a function of the chemical potential ($\mu - E_f$) at 500 K for different values of strain. The results obtained for S were expected. The increase in the electronic band gap induces an increase in the value of the Seebeck coefficient. Therefore, negative values of strain (compression) exhibit a larger Seebeck coefficient than positive values (expansion). Analyzing the behavior of S under strain could lead to conclusions with respect to electronic structure. For example, it can be seen
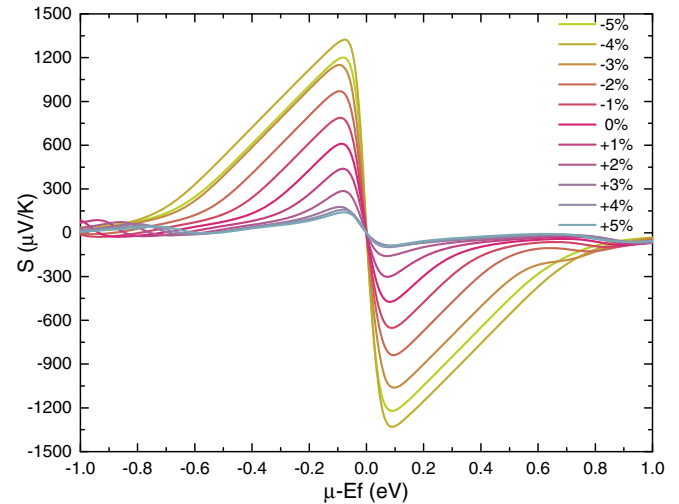
from the figure that +3%, +4%, and +5% strain show very similar behavior of S with respect to $\mu - E_f$. It is worth remembering the electronic transition mentioned above occurs at +3% of strain.

As mentioned, the trend observed is very clear; for higher biaxial expansion of the supercell smaller band gap and, therefore, a smaller value of Seebeck coefficient, except for -5% and -4%. It is observed that the maximum value of the Seebeck coefficient at -4% strain is larger than that at -5%, which is contrary to the overall trend. The only explanation for this behavior is that at such a value of strain, the band gap decreases. This means that the band gap at -4% strain is larger than at -5%. As mentioned above, InSe/GaSe superlattice without strain is a direct band-gap semiconductor. For negative values of strain, the valence band maximum slightly shifts away from the Γ point. However, at -5% strain, the conduction band minimum is no longer at the Γ point but at the K point. Under biaxial compression, the conduction band minimum at the Γ point moves to higher energies, which explains the increase in the band gap. However, this is not a rigid shift of the conduction bands. As can be seen in Fig. 3, from 0% to -3% strain, the conduction band minimum at Γ shifts more than 0.5 eV to higher energies while at K point exhibit a small drop in energy. Therefore, at -5% strain, the conduction band minimum is no longer at Γ and, starting at this compression, begins a new decrease of the band gap (see Fig. S4). Anisotropy in the superlattice could be responsible for this behavior.

A good value of the Seebeck coefficient is not enough to write a conclusion about the thermoelectric performance of a material. Under the constant relaxation time approximation, it is possible to obtain the ZT_e. This value can be obtained considering that the electrical conductivity is calculated over the relaxation time (σ/τ) as well as the electronic contribution to the thermal conductivity (κ_e/τ). This will give a better picture of the possible thermoelectric behavior under strain. Our results are shown in Fig. 6 for both types of doping at 500 K. It is very clear from the figure that the electronic thermoelectric performance decays with tensile strain. This is
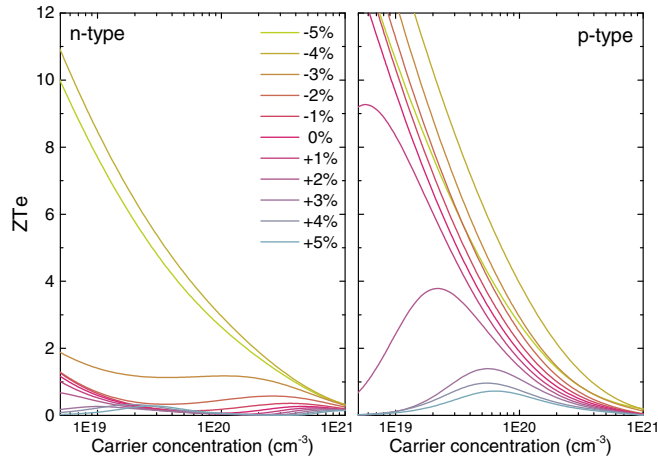
FIG. 6. Carrier concentration dependence of the ZT_e ($[S^2(\sigma/\tau)]/(\kappa_e/\tau)$) trace for InSe/GaSe superlattice at different values of strain and 500 K of temperature. The left panel shows *n*-type doping, while the right panel shows *p*-type doping.

FIG. 7. Trace of the lattice contribution to the thermal conductivity as a function of the temperature for three different strains −3%, 0%, and +3%.

because the improvement of the electrical conductivity due to the reduction of the band gap is not enough to overcome the drastic decrease of the Seebeck coefficient under this type of strain. With regard to the type of doping, our calculations suggest that the InSe/GaSe superlattice would exhibit its best thermoelectric performance with *p*-type doping. This can be due to the relatively flat valence bands that are at the vicinity of the gap. An unusual behavior for *n*-type doping appears at −4% strain. After this value of compressive strain, ZT_e exhibits similar values to that with *p*-type doping. This is due to what was mentioned above related to the nonlinear shift of the bands with strain. At the threshold of −4%, there is a change at the minimum conduction band, and even though unoccupied bands are still parabolic, the available states increase since there are two bands at almost the same energy (see Fig. 3).

The mentioned figure of merit, ZT_e, is just an approximation since the electronic relaxation time has not been calculated. However, it can give an estimation of the expected thermoelectric performance. Another key property for the full description of the thermoelectric figure of merit is the lattice contribution to the thermal conductivity. To obtain κ_l, it is necessary to calculate second- and third-order interatomic force constants. The second-order IFCs were obtained with the PHONOPY package [43] with a supercell of $4 \times 4 \times 2$. Since the InSe/GaSe superlattice is a layered system, the inclusion of van der Waals interactions may modify the dynamic properties, as shown in Ref. [60]. Therefore, the phonon-dispersion curves were obtained for the superlattice with DFT-D3 [61,62]. Figure S6 shows only minor differences, in the obtained frequencies, along specific high-symmetry branches when DFT-D3 and PBEsol are compared. Therefore, we considered that the PBEsol scheme is enough to describe the material's thermal properties correctly, and we do not find the use of DFT-D3 necessary. As such, we performed all the calculations related to second- and third-order interatomic force constants with the PBEsol approach. Dynamic stability under strain can be obtained through phonon calculations; the
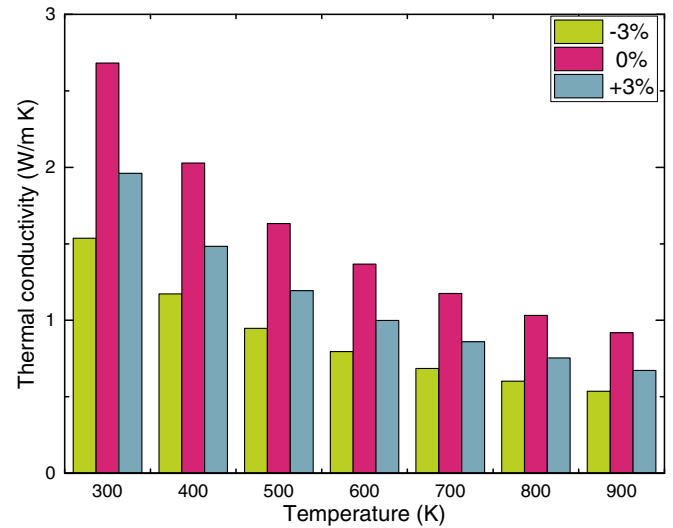
phonon dispersion curves were obtained for −3%, 0%, and +3% strain (see Fig. S5). The dispersion shows no negative phonons for any of the three applied strains, which indicates dynamic stability. For the third-order IFCs, the SHENGBTE code was used [44,45]. Interactions up to the tenth neighbor were taken into account in the calculation, and the distorted supercells created with the thirorder.py script [46] contain 64 atoms. Our results of the temperature dependence of the lattice contribution to the thermal conductivity are shown in Fig. 7. Our calculations indicate that negative strain reduces thermal conductivity. The average of the trace is very small, especially at high temperatures where the thermal conductivity approaches $1 \, \text{W m}^{-1} \text{K}^{-1}$. The anisotropy of the system yields anisotropic values of thermal conductivity. Figure S7 shows the overall trend of the in-plane and out-of-plane thermal conductivity for the superlattice at −3%, 0%, and +3% strain. As expected, the values for in plane and out of plane are very different. However, the thermal conductivity along the *c* direction does not show a tangible variation as a function of temperature. Our calculations indicate that, to improve thermoelectric performance in InSe/GaSe superlattices, the system should have *p*-type doping, and a negative biaxial strain should be applied. Compressive strain in the supercell increases the Seebeck coefficient and reduces thermal conductivity, which translated into an increase of ZT.

V. CONCLUSIONS

We have performed first principle calculations on superlattices of InSe/GaSe under biaxial in-plane tensile and compressive strain. Tensile strain closes the electronic gap, which induces a semiconductor-metal transition around 3% without the inclusion of SOC. However, with the inclusion of SOC, the band gap opens at the band crossing points, indicating a possible topological insulator behavior under strain. Therefore the inclusion of SOC is very important to capture the electronic behavior of this superlattice. With regard to

the electronic thermoelectric properties, the reduction of the band gap with tensile strain increases electrical conductivity; however, our calculations indicate that the increase in σ is not enough to overcome the decrease in Seebeck coefficient. The lattice contribution to the thermal conductivity decreases with compressive strain, which reinforces the conclusion that the best thermoelectric performance of superlattices of InSe/GaSe is achieved at negative strain. Our calculations show that the InSe/GaSe superlattice can be manipulated through biaxial strain to select the best thermoelectric performance at a given temperature. We expect that our results will motivate experimental groups to pursue the synthesis and characterization of this material and to focus on the effects of the electronic topology under biaxial strain.

[1] G. J. Snyder and E. S. Toberer, Complex thermoelectric materials, Nat. Mater. **7**, 105 (2008).

[2] *CRC Handbook of Thermoelectrics*, edited by D. M. Rowe (CRC Press, Boca Raton, 1995).

[3] H. J. Goldsmid, in *Recent Trends in Thermoelectric Materials Research I*, Semiconductors and Semimetals edited by T. M. Sbitt Vol. 69, (Elsevier, New York, 2001), pp. 1–24.

[4] T. M. Tritt and M. A. Subramanian, Thermoelectric materials, phenomena, and applications: A bird's eye view, MRS Bull. **31**, 188 (2006).

[5] J. Yang and T. Caillat, Thermoelectric materials for space and automotive power generation, MRS Bull. **31**, 224 (2006).

[6] S. I. Kim, K. H. Lee, H. A. Mun, H. S. Kim, S. W. Hwang, J. W. Roh, D. J. Yang, W. H. Shin, X. S. Li, Y. H. Lee, G. J. Snyder, and S. W. Kim, Dense dislocation arrays embedded in grain boundaries for high-performance bulk thermoelectrics, Science **348**, 109 (2015).

[7] G. Tan, L.-D. Zhao, and M. G. Kanatzidis, Rationally designing high-performance bulk thermoelectric materials, Chem. Rev. **116**, 12123 (2016).

[8] M. Dresselhaus, G. Chen, M. Tang, R. Yang, H. Lee, D. Wang, Z. Ren, J.-P. Fleurial, and P. Gogna, New directions for low-dimensional thermoelectric materials, Adv. Mater. **19**, 1043 (2007).

[9] L.-D. Zhao, V. P. Dravid, and M. G. Kanatzidis, The panoscopic approach to high performance thermoelectrics, Energy Environ. Sci. **7**, 251 (2014).

[10] L.-D. Zhao, G. Tan, S. Hao, J. He, Y. Pei, H. Chi, H. Wang, S. Gong, H. Xu, V. P. Dravid, C. Uher, G. J. Snyder, C. Wolverton, and M. G. Kanatzidis, Ultrahigh power factor and thermoelectric performance in hole-doped single-crystal SnSe, Science **351**, 141 (2016).

[11] A. T. Duong, V. Q. Nguyen, G. Duvjir, V. T. Duong, S. Kwon, J. Y. Song, J. K. Lee, J. E. Lee, S. Park, T. Min, J. Lee, J. Kim, and S. Cho, Achieving ZT = 2.2 with Bi-doped n-type SnSe single crystals, Nat. Commun. **7**, 13713 (2016).

[12] L.-D. Zhao, S.-H. Lo, Y. Zhang, H. Sun, G. Tan, C. Uher, C. Wolverton, V. P. Dravid, and M. G. Kanatzidis, Ultralow thermal conductivity and high thermoelectric figure of merit in SnSe crystals, Nature (London) **508**, 373 (2014).

[13] A. Dewandre, O. Hellman, S. Bhattacharya, A. H. Romero, G. K. H. Madsen, and M. J. Verstraete, Two-Step Phase Transition in SnSe and the Origins of Its High Power Factor from First Principles, Phys. Rev. Lett. **117**, 276601 (2016).

[14] U. Aseginolaza, R. Bianco, L. Monacelli, L. Paulatto, M. Calandra, F. Mauri, A. Bergara, and I. Errea, Phonon Collapse and Second-Order Phase Transition in Thermoelectric SnSe, Phys. Rev. Lett. **122**, 075901 (2019).

[15] S. Tang and M. S. Dresselhaus, Anisotropic transport for parabolic, non-parabolic, and linear bands of different dimensions, Appl. Phys. Lett. **105**, 033907 (2014).

[16] C. Wan, Y. Wang, N. Wang, W. Norimatsu, M. Kusunoki, and K. Koumoto, Development of novel thermoelectric materials by reduction of lattice thermal conductivity, Sci. Tech. Adv. Mater. **11**, 044306 (2010).

[17] R. Venkatasubramanian, E. Siivola, T. Colpitts, and B. O'Quinn, Thin-film thermoelectric devices with high room-temperature figures of merit, Nature (London) **413**, 597 (2001).

[18] W. Ibarra-Hernández, H. Elsayed, A. H. Romero, A. Bautista-Hernández, D. Olguín, and A. Cantarero, Electronic structure, lattice dynamics, and optical properties of a novel van der Waals semiconductor heterostructure: InGaSe$_2$, Phys. Rev. B **96**, 035201 (2017).

[19] A. S. Kumar, M. Wang, Y. Li, R. Fujita, and X. P. A. Gao, Interfacial charge transfer and gate-induced hysteresis in monochalcogenide InSe/GaSe heterostructures, ACS Appl. Mater. Interfaces **12**, 46854 (2020).

[20] X. Li, M.-W. Lin, A. A. Puretzky, J. C. Idrobo, C. Ma, M. Chi, M. Yoon, C. M. Rouleau, I. I. Kravchenko, D. B. Geohegan, and K. Xiao, Controlled vapor phase growth of single crystalline,

two-dimensional GaSe crystals with high photoresponse, Sci. Rep. **4**, 5497 (2014).

[21] X. Li, L. Basile, M. Yoon, C. Ma, A. A. Puretzky, J. Lee, J. C. Idrobo, M. Chi, C. M. Rouleau, D. B. Geohegan, and K. Xiao, Revealing the preferred interlayer orientations and stackings of two-dimensional bilayer gallium selenide crystals, Angew. Chem., Int. Ed. **54**, 2712 (2015).

[22] A. Koma, Van der Waals epitaxy—a new epitaxial growth method for a highly lattice-mismatched system, Thin Solid Films **216**, 72 (1992).

[23] J. E. Palmer, T. Saitoh, T. Yodo, and M. Tamura, Growth and characterization of GaSe and GaAs/GaSe on As-passivated Si(111) substrates, J. Appl. Phys. **74**, 7211 (1993).

[24] L. T. Vinh, M. Eddrief, C. Sébenne, A. Sacuto, and M. Balkanski, Heteroepitaxy of GaSe layered semiconductor compound on *Si*(111) 7×7 substrate: a Van der Waals epitaxy?, J. Cryst. Growth **135**, 1 (1994).

[25] Y. Zheng, A. Köebel, J. Pétroff, J. Boulliard, B. Capelle, and M. Eddrief, GaSeSi(111) heteroepitaxy: the early stages of growth, J. Cryst. Growth **162**, 135 (1996).

[26] K. Ueno, H. Abe, K. Saiki, and A. Koma, Heteroepitaxy of layered semiconductor GaSe on a GaAs(111)B surface, Jpn. J. Appl. Phys. **30**, L1352 (1991).

[27] A. Ludviksson, L. Rumaner, J. Rogers, and F. Ohuchi, Vacuum sublimation of GaSe: a molecular source for deposition of GaSe, J. Cryst. Growth **151**, 114 (1995).

[28] M. Hajji, H. Absike, H. Labrim, H. Ez-Zahraouy, M. Benaissa, and A. Benyoussef, Strain effects on the electronic and thermoelectric properties of Bi_2Te_3: A first principles study, Comput. Condens. Matter **16**, e00299 (2018).

[29] Z. Kerrami, A. Sibari, O. Mounkachi, A. Benyoussef, and M. Benaissa, SnO_2 improved thermoelectric properties under compressive strain, Comput. Condens. Matter **18**, e00356 (2019).

[30] Q. Wang, L. Han, L. Wu, T. Zhang, S. Li, and P. Lu, Strain effect on thermoelectric performance of InSe monolayer, Nanoscale Res. Lett. **14**, 287 (2019).

[31] G. Kresse and J. Furthmüller, Efficient iterative schemes for *ab initio* total-energy calculations using a plane-wave basis set, Phys. Rev. B **54**, 11169 (1996).

[32] P. Hohenberg and W. Kohn, Inhomogeneous Electron Gas, Phys. Rev. **136**, B864 (1964).

[33] W. Kohn and L. J. Sham, Self-Consistent Equations Including Exchange and Correlation Effects, Phys. Rev. **140**, A1133 (1965).

[34] G. Kresse and D. Joubert, From ultrasoft pseudopotentials to the projector augmented-wave method, Phys. Rev. B **59**, 1758 (1999).

[35] J. P. Perdew, K. Burke, and M. Ernzerhof, Generalized Gradient Approximation Made Simple, Phys. Rev. Lett. **77**, 3865 (1996).

[36] H. J. Monkhorst and J. D. Pack, Special points for Brillouin-zone integrations, Phys. Rev. B **13**, 5188 (1976).

[37] J. Sun, A. Ruzsinszky, and J. P. Perdew, Strongly Constrained and Appropriately Normed Semilocal Density Functional, Phys. Rev. Lett. **115**, 036402 (2015).

[38] A. D. Becke and E. R. Johnson, A simple effective potential for exchange, J. Chem. Phys. **124**, 221101 (2006).

[39] F. Tran and P. Blaha, Accurate Band Gaps of Semiconductors and Insulators with a Semilocal Exchange-Correlation Potential, Phys. Rev. Lett. **102**, 226401 (2009).

[40] G. K. H. Madsen, J. Carrete, and M. J. Verstraete, BoltzTraP2, a program for interpolating band structures and calculating semi-classical transport coefficients, Comput. Phys. Commun. **231**, 140 (2018).

[41] T. J. Scheidemantel, C. Ambrosch-Draxl, T. Thonhauser, J. V. Badding, and J. O. Sofo, Transport coefficients from first-principles calculations, Phys. Rev. B **68**, 125210 (2003).

[42] W. Ibarra-Hernández, M. J. Verstraete, and J.-Y. Raty, Effect of hydrostatic pressure on the thermoelectric properties of Bi_2Te_3, Phys. Rev. B **90**, 245204 (2014).

[43] A. Togo and I. Tanaka, First principles phonon calculations in materials science, Scr. Mater. **108**, 1 (2015).

[44] W. Li, J. Carrete, N. A. Katcho, and N. Mingo, ShengBTE: A solver of the Boltzmann transport equation for phonons, Comput. Phys. Commun. **185**, 1747 (2014).

[45] W. Li, N. Mingo, L. Lindsay, D. A. Broido, D. A. Stewart, and N. A. Katcho, Thermal conductivity of diamond nanowires from first principles, Phys. Rev. B **85**, 195436 (2012).

[46] W. Li, L. Lindsay, D. A. Broido, D. A. Stewart, and N. Mingo, Thermal conductivity of bulk and nanowire $Mg_2Si_xSn_{1-x}$ alloys from first principles, Phys. Rev. B **86**, 174307 (2012).

[47] S. Li, Z. Tong, and H. Bao, Resolving different scattering effects on the thermal and electrical transport in doped SnSe, J. Appl. Phys. **126**, 025111 (2019).

[48] D. Errandonea, A. Segura, F. J. Manjón, A. Chevy, E. Machado, G. Tobias, P. Ordejón, and E. Canadell, Crystal symmetry and pressure effects on the valence band structure of γ-InSe and ϵ-GaSe: Transport measurements and electronic structure calculations, Phys. Rev. B **71**, 125206 (2005).

[49] F. M. Gashimzade and N. B. Mustafaev, Energy spectrum and effective mass of carriers in the InSe/GaSe superlattice, Z. Phys. B: Condens. Matter **99**, 219 (1995).

[50] T. Hu, J. Zhou, and J. Dong, Strain induced new phase and indirect-direct band gap transition of monolayer InSe, Phys. Chem. Chem. Phys. **19**, 21722 (2017).

[51] Y. Ma, Y. Dai, M. Guo, L. Yu, and B. Huang, Tunable electronic and dielectric behavior of GaS and GaSe monolayers, Phys. Chem. Chem. Phys. **15**, 7098 (2013).

[52] See Supplemental Material at http://link.aps.org/supplemental/10.1103/PhysRevMaterials.6.025403 for additional information of SOC effect, bands obtained with scan, phonon dispersion curves, and detailed thermal conductivity.

[53] G. W. Mudd, S. A. Svatek, T. Ren, A. Patanè, O. Makarovsky, L. Eaves, P. H. Beton, Z. D. Kovalyuk, G. V. Lashkarev, Z. R. Kudrynskyi, and A. I. Dmitriev, Tuning the bandgap of exfoliated InSe nanosheets by quantum confinement, Adv. Mater. **25**, 5714 (2013).

[54] V. Zólyomi, N. D. Drummond, and V. I. Fal'ko, Electrons and phonons in single layers of hexagonal indium chalcogenides from *ab initio* calculations, Phys. Rev. B **89**, 205416 (2014).

[55] G. W. Mudd, M. R. Molas, X. Chen, V. Zólyomi, K. Nogajewski, Z. R. Kudrynskyi, Z. D. Kovalyuk, G. Yusa, O. Makarovsky, L. Eaves, M. Potemski, V. I. Fal'ko, and A. Patanè, The direct-to-indirect band gap crossover in two-dimensional van der Waals indium selenide crystals, Sci. Rep. **6**, 39619 (2016).

[56] T. Cao, Z. Li, and S. G. Louie, Tunable Magnetism and Half-Metallicity in Hole-Doped Monolayer GaSe, Phys. Rev. Lett. **114**, 236602 (2015).

[57] B. Sa, J. Zhou, Z. Sun, J. Tominaga, and R. Ahuja, Topological Insulating in GeTe/Sb$_2$Te$_3$ Phase-Change Superlattice, Phys. Rev. Lett. **109**, 096802 (2012).

[58] Z. Zhu, Y. Cheng, and U. Schwingenschlögl, Topological Phase Transition in Layered GaS and GaSe, Phys. Rev. Lett. **108**, 266805 (2012).

[59] J. Sun, R. C. Remsing, Y. Zhang, Z. Sun, A. Ruzsinszky, H. Peng, Z. Yang, A. Paul, U. Waghmare, X. Wu, M. L. Klein, and J. P. Perdew, Accurate first-principles structures and energies of diversely bonded systems from an efficient density functional, Nat. Chem. **8**, 831 (2016).

[60] S. Li, X. Zhang, and H. Bao, Thermal transport by electrons and phonons in PdTe$_2$: an *ab initio* study, Phys. Chem. Chem. Phys. **23**, 5956 (2021).

[61] S. Grimme, J. Antony, S. Ehrlich, and H. Krieg, A consistent and accurate *ab initio* parametrization of density functional dispersion correction (DFT-D) for the 94 elements H-Pu, J. Chem. Phys. **132**, 154104 (2010).

[62] S. Grimme, S. Ehrlich, and L. Goerigk, Effect of the damping function in dispersion corrected density functional theory, J. Comput. Chem. **32**, 1456 (2011).